**Indonesian Journal of Electrical Engineering and Computer Science**
Vol. 43, No. 1, July 2026, pp. 39~62
ISSN: 2502-4752, DOI: 10.11591/ijeecs.v43.i1.pp39-62


# Adaptive vector control of PV-fed induction motor using boost split-source inverter without MPPT

**Romaissa Hamdi[1], Yassine Beddiaf[2], Djamel Sakri[3], Daoud Rezzak[2], Hassina Slimani[1]**
[1]SATIT Laboratory, Faculty of Science and Technology, Abbes Laghrour University of Khenchela, Khenchela, Algeria
[2]LTIMER Laboratory, Faculty of Science and Technology, Abbes Laghrour University of Khenchela, Khenchela, Algeria
[3]Department of Electrical Engineering, Faculty of Science and Technology, University Oum El Bouaghi, Oum El Bouaghi, Algeria

**Article Info**

***Article history:***

Received Mar 8, 2026
Revised Jun 3, 2026
Accepted Jun 27, 2026

***Keywords:***

Adaptive API controller
Boost split-source inverter
Photovoltaic system
Sliding mode control
Vector control of IM

**ABSTRACT**

This paper proposes an adaptive vector control strategy for a photovoltaic (PV)-fed induction motor using a boost split-source inverter (BSSI). Unlike conventional PV conversion systems, the proposed topology combines voltage boosting and DC–AC conversion in a single stage, reducing component count, switching losses, and overall system complexity. In addition, the system operates without a maximum power point tracking (MPPT) algorithm, simplifying the control structure while maintaining stable operation under varying environmental conditions. The proposed control approach integrates sliding mode control (SMC) for robust DC-bus voltage regulation and an adaptive proportional–integral (API) speed controller based on Lie derivative theory for online tuning of controller gains according to the speed tracking error. An active DC-link protection mechanism is also introduced to prevent overvoltage during transient conditions. The main contribution of this paper lies in the combination of the BSSI topology with a hybrid adaptive control framework to improve robustness, dynamic performance, and system reliability under irradiance, temperature, and load variations. Simulation and experimental results demonstrate fast dynamic response, reduced speed and voltage oscillations, accurate speed tracking, and superior performance compared with conventional vector control methods.

*This is an open access article under the CC BY-SA license.*

***Corresponding Author:***

Yassine Beddiaf
LTIMER Laboratory, Faculty of Science and Technology, Abbes Laghrour University of Khenchela
Khenchela, Algeria
Email: beddiaf.yassine@univ-khenchela.dz

## 1. INTRODUCTION

Photovoltaic (PV) systems have experienced rapid development due to the global transition toward renewable energy sources and the need to reduce dependence on fossil fuels. The integration of solar energy into electrical power systems requires efficient and robust energy conversion solutions, capable of ensuring both DC-bus stability and the reliability of supplied loads. In this context, the use of inverters for supplying electrical machines, such as the boost split-source inverter (BSSI), combined with robust control strategies, represents a promising approach to improve the overall performance of PV chains.

In this context, the Z-source inverter (ZSI) proposed by Peng [1] was adopted to minimize the number of conversion stages, provide buck–boost functionality, and reduce the overall number of components. However, achieving shoot-through states requires additional switching actions, slightly increasing the complexity of the control strategy. Recently, a single-stage three-phase boost inverter topology, known as the split-source inverter (SSI), was introduced by Lee and Heng [2]. This topology

simplifies the simultaneous control of the DC-bus voltage and the AC output within a single-stage structure, while avoiding undesired high-frequency switching and enabling a wide AC voltage range in both buck and boost modes. In the proposed configuration, an inductor is connected to two metal-oxide-semiconductor field-effect transistors (MOSFETs) operating at the fundamental frequency to elevate the input voltage to the DC-bus, while a hybrid quasi-sinusoidal and constant duty-cycle modulation simultaneously controls inductor charging and AC voltage generation. To overcome the limitations of the classical SSI, Yin *et al.* [3] proposed a modified split-source inverter (MSSI) capable of performing dual power decoupling, utilizing both DC- and AC-side capacitors to divert second-order ripples, which is particularly important for photovoltaic or other ripple-sensitive sources.

Moreover, Abd-Elaziz *et al.* [4] demonstrated that SSIs are promising candidates for high-gain single-stage DC–AC converters, suitable for interfacing PV modules with electrical grids and AC loads, using a finite control set model predictive control (FCS-MPC) strategy without pulse-width modulation. Kumar and Sensarma [5] highlight the need for buck-boost inverters when the source voltage is low relative to the AC output voltage, a common requirement in solar micro-inverters. In Miyani *et al.* [6], a discrete-time sliding mode (DTSM) regulator was proposed for regulating the DC-bus voltage of a quasi-Z-source inverter (q-ZSI) in a three-phase grid-connected PV system. The DC-bus voltage of the q-ZSI exhibits non-minimum phase behavior, complicating controller design. The DTSM controller is implemented in a dual-loop architecture, regulating the DC voltage in the outer loop and the inductor current in the inner loop, with the shoot-through duty ratio determined by the inner loop. Borges and Grigoletto [7] demonstrated the effectiveness of DTSM for a three-phase grid-connected q-ZSI, ensuring robustness and grid compliance despite the non-minimum phase behavior of the DC-link voltage. In Dabour *et al.* [8], the SSI concept was extended with quadratic boost SSI (QBI/SBI) topologies, using an additional inductor, capacitor, and two diodes to square the boosting factor of the SSI. A closed-loop control strategy, combined with modified space vector modulation (MSVM), was used to reduce input current ripples.

Mahmmoud *et al.* [9] present an integrated daytime solar system designed to supply a three-phase induction motor, with the PV array directly feeding a SSI. The incremental conductance (INC) method was employed for maximum power point tracking (MPPT). Building on this work, Sabrié *et al.* [10] proposed a SSI-derived topology, named B-ASSI, aiming to improve DC voltage utilization while retaining the structural advantages of the SSI. Furthermore, Dabour *et al.* [11] introduced an indirect field-oriented control (IFOC) for a five-phase induction motor supplied by a SSI. Wageh *et al.* [12] propose a normalized space vector modulation (SVPWM) technique for a four-switch three-phase voltage source inverter (FSTP-VSI), capable of maintaining satisfactory performance even in the presence of voltage fluctuations, using stator voltages in the stationary reference frame. Moreover, Ibrahim *et al.* [13] investigate the design, analytical modeling, and experimental validation of a SSI topology intended for high-gain DC–AC power conversion with reduced power losses. The authors introduce an advanced control strategy based on space vector modulation (SVM), which enables the generation of near-sinusoidal output voltages with low harmonic distortion. Abdulhussein and Gün [14] proposed a three-phase buck–BSSI for the integration of low-voltage renewable energy sources, such as photovoltaic systems and fuel cells, into medium-voltage AC grids. The proposed topology enhances the voltage boosting capability while reducing the voltage stress across the power switches.

In Monjo *et al.* [15], a comprehensive stability assessment of grid-connected photovoltaic systems employing a quasi-Z-source inverter (q-ZSI) was presented. The authors developed detailed dynamic models to investigate the interactions between the converter and the electrical network under transient operating conditions. Their analysis identified several factors that may compromise system stability and highlighted suitable control and design measures to improve damping characteristics and maintain stable grid integration. In Abd-Elaziz *et al.* [16], a stand-alone photovoltaic power generation system integrating a SSI and a battery energy storage unit was developed to improve the reliability of off-grid electrification applications. The proposed architecture eliminates the need for a separate DC–DC conversion stage, thereby reducing system complexity, size, and implementation cost. Furthermore, a detailed small-signal dynamic model was established to facilitate controller design and stability assessment. In Lotfy *et al.* [17], an advanced high-gain variant of the SSI was presented to overcome the limited voltage boosting capability of conventional single-stage inverter structures. The proposed topology incorporates a dedicated voltage-enhancement network based on passive energy-storage elements, allowing a significant increase in the conversion ratio while preserving the simplicity of the overall system. To further improve performance, an independent current regulation scheme was developed, enabling separate control of the source-side and load-side currents. Moreover, an adapted space vector modulation method was employed to achieve smoother current waveforms and better switching behavior.

In this context, conventional PV-fed induction motor systems generally rely on multi-stage power conversion structures associated with MPPT algorithms to regulate the photovoltaic energy flow and ensure stable motor operation. However, these approaches increase the overall system complexity, switching losses,

and implementation cost.To address these limitations, this paper proposes a single-stage BSSI-based architecture that simultaneously performs voltage boosting and DC–AC conversion without requiring an MPPT algorithm. In addition, an innovative vector control strategy for the induction motor is developed to ensure precise speed regulation and robust operation under varying environmental and load conditions. The proposed approach combines robust DC-link regulation with adaptive speed control, enhancing system reliability while reducing control complexity. Furthermore, a DC-bus protection mechanism is implemented to improve the safety and stability of the overall PV conversion chain. Table 1 summarizes the most commonly used inverter topologies in PV-fed motor drive systems, highlighting their control strategies, advantages, and limitations

The paper is organized as follows: section 1 presents the introduction, including the background, motivation, and a review of relevant literature on PV-driven motor systems and inverter topologies. Section 2 presents the general configuration of the control strategy for IM-BSSI in PV chain. Section 3 focuses on the modified vector control strategy of IM-BSSI, explaining the implementation of the SMC and adaptive proportional-integral (API) controller. Section 4 introduces the protection scheme for the DC-bus. Section 5 presents the simulation and experimental results, demonstrating the effectiveness, robustness, and performance of the proposed approach. The paper concludes with Section 6, summarizing the main outcomes and highlighting the contributions.

Table 1. Comparative table summarizing inverter topologies, control strategies, and limitations

| Inverter topology | Control strategy | Main advantages | Limitations |
|---|---|---|---|
| Conventional VSI | SPWM/SVPWM + MPPT | Simple and mature structure, high efficiency | Requires DC-DC stage for PV adaptation, strong dependence on MPPT |
| PV + Boost converter + VSI | MPPT + PWM control | Effective PV power extraction, stabilized DC-link voltage | Multi-stage architecture, increased control complexity |
| Z-source inverter (ZSI) | Shoot-through control + PWM | Integrated voltage boost without DC-DC converter, flexible operation | Output current ripple, complex control design |
| Quasi-Z-source inverter (q-ZSI) | Improved shoot-through control | Reduced input current stress, improved continuity | Non-minimum phase behavior, challenging dynamic response |
| Proposed system (PV + integrated boost + robust control) | Robust control (PI/RST or equivalent), no separate MPPT stage | Reduced system complexity, integrated conversion stages, improved robustness | Requires precise tuning and experimental validation |

## 2. GENERAL CONFIGURATION OF THE CONTROL STRATEGY FOR IM-BSSI IN PV CHAIN

Figure 1 depicts the architecture of the proposed photovoltaic-based system intended for driving a three-phase induction motor. The configuration integrates a photovoltaic generator with an induction motor–BSSI, forming a compact and efficient energy conversion structure. All subsystems are electrically coupled and controlled through a robust hybrid control scheme that combines sliding mode control (SMC) with an adaptive controller formulated using Lie derivative-based design.

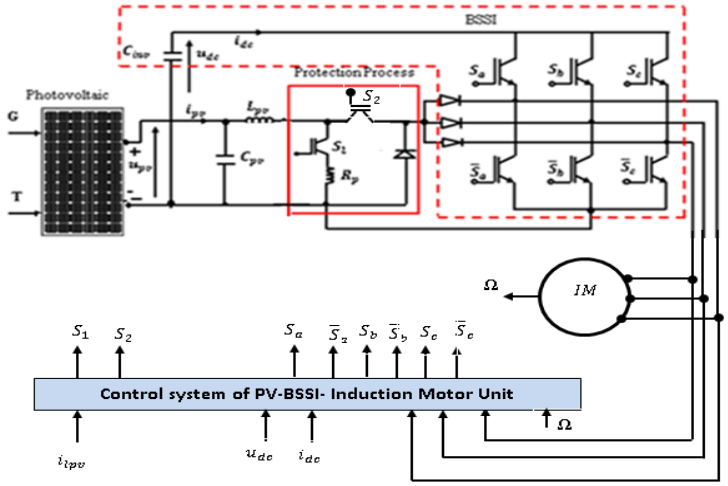



Figure 1. New design configuration of the photovoltaic chain

This unified control framework enables simultaneous voltage boosting of the photovoltaic output, DC–AC power conversion via the inverter stage, and precise regulation of the induction motor drive. Furthermore, a dedicated protection strategy is incorporated to mitigate DC-link overvoltage conditions, thereby enhancing the operational safety and reliability of the overall system. The subsequent sections present a detailed modeling, control design, and analysis of each component within the proposed configuration

### 2.1. Mathematical model of the PV

To thoroughly analyze the operation of the proposed system, it is essential to conduct a detailed study of the energy source, namely the photovoltaic panel. Therefore, we begin with its mathematical modeling. Figure 2 shows the equivalent circuit diagram of a photovoltaic cell [18], [19].

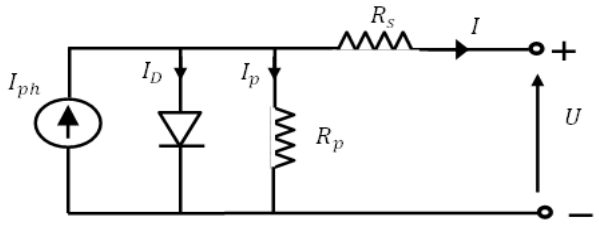



Figure 2. Equivalent circuit diagram of a photovoltaic cell

According to the equivalent circuit shown in Figure 2, the output current of the cell is given by:

$$I = I_{ph} - I_D - I_p \tag{1}$$

The photocurrent $I_{ph}$ mainly depends on two parameters: solar irradiance and temperature, and is given by:

$$I_{ph} = I_{ph-STC}\frac{G}{G_{STG}}\left(1 + k_i(T - T_{STC})\right) \tag{2}$$

where $G$ is the solar irradiation measured, $G_{STG}$ is the solar irradiation in standard conditions ($1\ kW/m^2$), $T_{STC}$ is the temperature under standard test conditions (298.15 K), $k_i$ is the current coefficient.

The diode current $I_D$ is expressed according to its current–voltage characteristic and is given by:

$$I_D = I_0\left(e^{\frac{q(U+R_sI)}{a.k.T}} - 1\right) \tag{3}$$

where $R_s$ is the equivalent series resistance of the photocell (Ω). $T$ is the real temperature of the p-n junction (K). $a$ is the ideality constant of the diode. $k$ is the Boltzmann constant ($1.38.10^{-23}$ J/K), and $q$ is the electron charge ($1.602.10^{--19}$ C).

The current $I_p$ is derived by applying Kirchhoff's current law:

$$I_p = \frac{U+R_S.I_D}{R_p} \tag{4}$$

where $R_p$ is the equivalent parallel resistance (Ω).

For a panel consisting of $N_s$ series cells and $N_p$ parallel cells, the output current can be determined by:

$$I = I_{ph-STC}\frac{G}{G_{STG}}(1 + k_i\Delta T) - I_0\left(e^{\frac{q\left(U+R_s\left(\frac{N_s}{N_p}\right)I\right)}{a.k.T.N_s}} - 1\right) - \frac{U+R_s\left(\frac{N_s}{N_p}\right).I_D}{R_p.\left(\frac{N_s}{N_p}\right)} \tag{5}$$

Based on the mathematical model (5), the current–voltage and power–voltage characteristics of the solar panel can be described through simulation using MATLAB. Table 2 presents the values of the panel's various parameters extracted from the MATLAB library (from the: Solar World SW165 mono software).

Table 2. Values of the panel's various parameters

| $U_{pm}$ | $I_{pm}$ | $P_{max,m}$ | $I_{sc}$ | $U_{co,n}$ | $I_{pv,n}$ | $a$ | $R_p$ | $R_s$ | $k_v$ | $k_i$ | $N_s$ |
|---|---|---|---|---|---|---|---|---|---|---|---|
| 35 V | 4.71A | 164.85 W | 5.25 A | 43.5 V | 5.27 A | 1.021 | 125 Ω | 0.628 Ω | 0.39V/K | 0.03A/K | 72 |

The simulation results of the developed model are presented in Figures 3 and 4. Figure 3 highlights the current-voltage characteristic ($I = f(V)$), while Figure 4 illustrates the power-voltage characteristic ($P = f(V)$). These curves provide insight into the electrical behavior of the photovoltaic panel under various solar irradiation ($0.1\ kW/m^2$ to $1\ kW/m^2$). The current-voltage in Figure 3 shows the effect of solar irradiation variation on the current for a given voltage. Indeed, an increase in irradiation leads to a significant rise in the generated current, while a decrease results in a lower current value. A similar observation can be made for the power-voltage characteristic as shown in Figure 4. An increase in solar irradiation results in a higher maximum power output from the module, while a decrease in irradiation leads to reduced power generation. Figure 5 illustrates the effect of temperature on the power output of the panel. It is observed that as the temperature increases, the maximum power decreases, highlighting the negative impact of temperature on the performance of the photovoltaic module. These results confirm the strong dependence of photovoltaic panel performance on solar irradiance and temperature conditions.

The operation of the proposed BSSI system is structured around two fundamental phases: the coil charging phase and the discharging phase. During the charging stage, energy is stored in the inductor through the controlled activation of the power switches. In the discharging stage, this stored energy is subsequently transferred to the load or to the next stage of the converter, ensuring efficient and stable power conversion. These two tightly synchronized phases are essential for achieving high performance, optimal efficiency, and robust dynamic behavior of the BSSI.

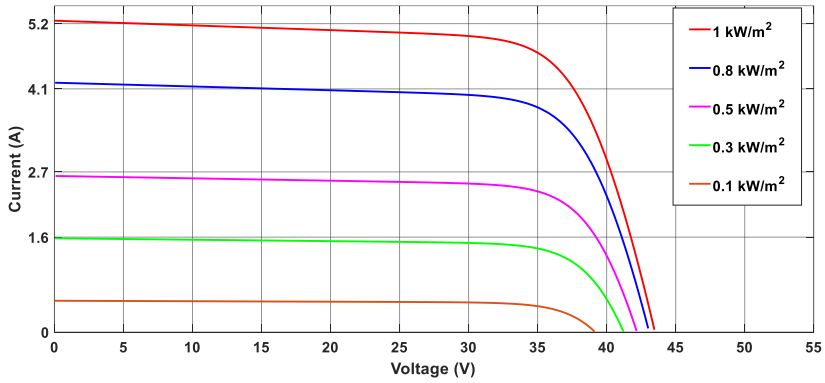



Figure 3. I-V characteristics for different solar irradiation values of the solar world PV module

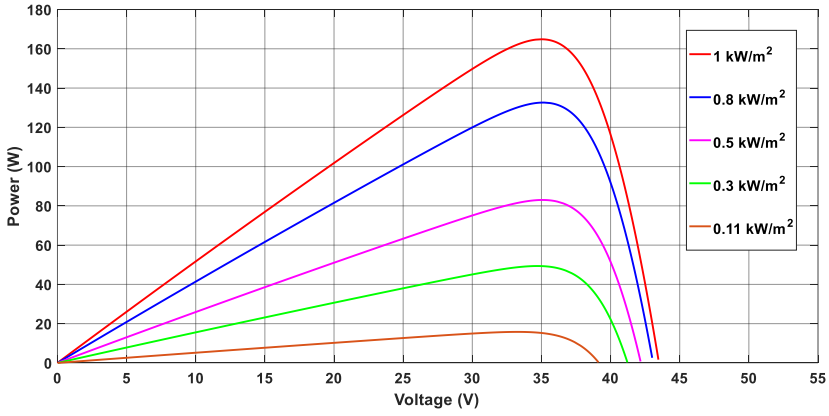



Figure 4. P-V characteristics for different solar irradiation values of the solar world PV module

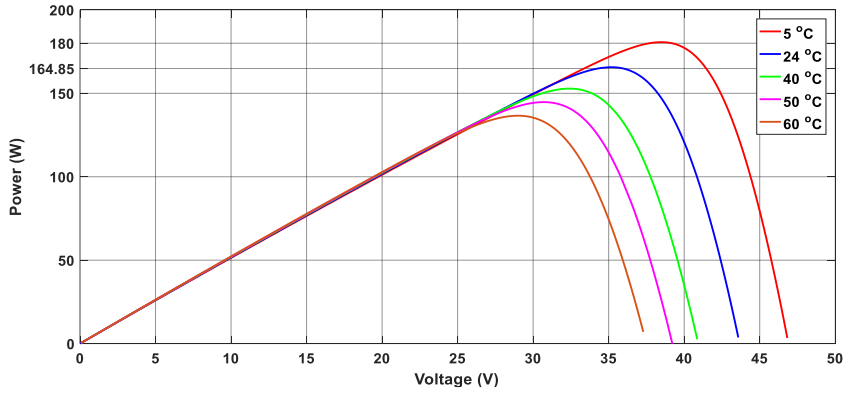



Figure 5. P-V characteristics for different ambient temperature values of the solar world PV module

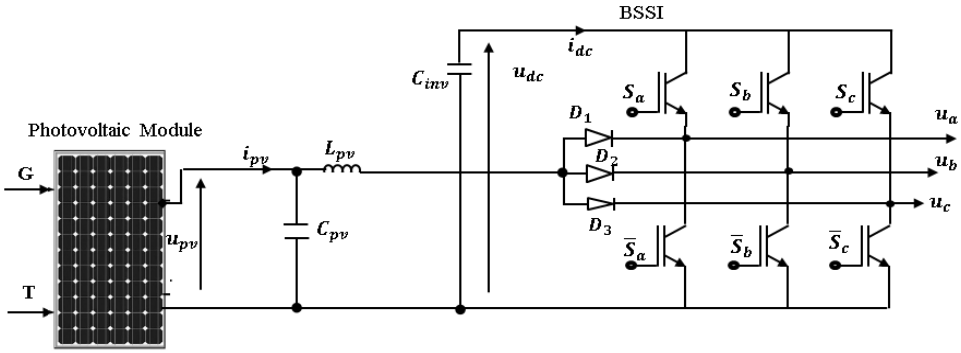



Figure 6. Boost split source inverter topology

### 2.2.1. Phase 1: inductor charging

As shown in Figure 7, the appropriate bridge switch is activated so that the input source is connected to the inductive branch. Energy is thereby stored in the inductor $L_{pv}$, while the DC-link capacitor contributes to maintaining the output voltage.

The voltage at the DC-side output is zero due to the short-circuit condition. In this mode, diode $D_1$ is conducting, as illustrated in Figure 7. Consequently, the inductor $L_{pv}$ is charged. By applying Kirchhoff's Voltage Law under steady-state conditions, the expressions of the charging current and voltage can be derived:

$$\begin{cases} V_{L_{pv}} = u_{pv} \\ i_{Lpv} = i_{pv} - i_{C_{pv}} \\ i_{C_{pv}} = C_{pv}\frac{du_{pv}}{dt} \\ i_{dc} = C_{inv}\frac{du_{dc}}{dt} \\ \frac{di_{pv}}{dt} = \frac{u_{pv}}{L_{pv}} \end{cases} \quad (6)$$

By taking the inductor current $i_{L_{pv}}$ and the capacitor voltage $u_{dc}$ as the state variables, the state vector can be defined as: $x(t) = [i_{L_{pv}} \quad u_{dc}]^T$, The input and output variables are defined by: $u(t) = [u_{pv} \quad i_{dc}]^T$ , the (6) can be write:

$$\dot{x} = A_{ch}x + B_{ch}u \quad (7)$$

where: $A_{ch} = \begin{bmatrix} 0 & 0 \\ 0 & 0 \end{bmatrix}$, $B_{ch} = \begin{bmatrix} \frac{1}{L_{pv}} & 0 \\ 0 & \frac{1}{C_{inv}} \end{bmatrix}$

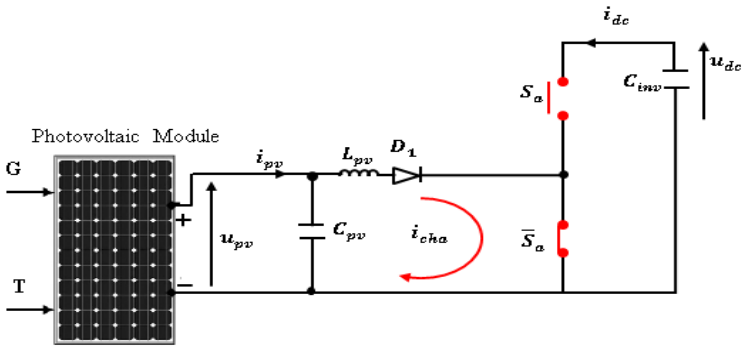



Figure 7. Inductive charging stage

### 2.2.2. Phase 2: inductor discharging and conversion

During this phase, the energy stored in the inductor is transferred to the DC-bus and delivered to the inverter bridge. The combined action of $L_{pv}$ discharging and the capacitor $C_{inv}$ ensures voltage boosting (boost mode) as shown in Figure 8.

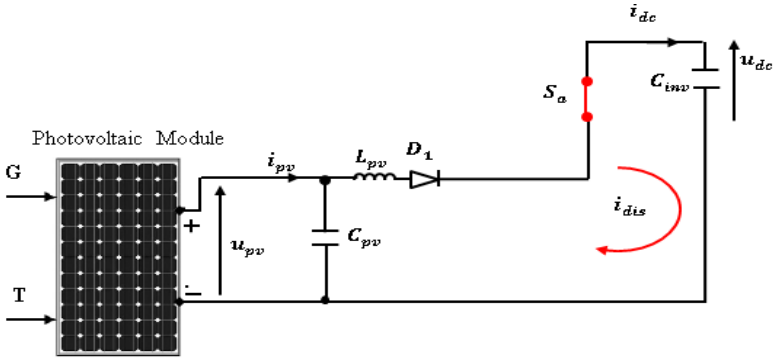



Figure 8. Inductive discharging phase

During this stage, the following relationships are obtained as a function of the discharging duty cycle, defined as $D_{dis} = 1 - D_{ch}$. By applying Kirchhoff's Voltage Law, we obtain:

$$V_{L_{pv}} = u_{pv} - u_{dc} \tag{8}$$

The volt-second balance (over one switching period) is given by:

$$D_{ch} V_{L_{pv}} + D_{dis}\left(u_{pv} - u_{dc}\right) = 0 \tag{9}$$

Therefore:

$$u_{dc} = \frac{u_{pv}}{D_{dis}} \tag{10}$$

The current balance is given by:

$$i_{dc} = D_{dis} i_{L_{pv}} \tag{11}$$

The (9-10) can be rewritten as:

$$\dot{x} = A_{dis} x + B_{dis} u \tag{12}$$

where: $A_{dis} = \begin{bmatrix} 0 & \frac{-1}{L_{pv}} \\ 0 & 1 \end{bmatrix}$, $B_{dis} = \begin{bmatrix} \frac{1}{L_{pv}} & 0 \\ 0 & -C_{pv} \end{bmatrix}$

Inductor current ripple during charging and discharging:

$$\begin{cases} \Delta i_{L_{pv}}\big|_{dis} = \frac{D_{dis}(u_{pv}-u_{dc})}{L_{pv}} T_s \\ \Delta i_{L_{pv}}\big|_{ch} = \frac{D_{ch}u_{pv}}{L_{pv}} T_s \end{cases} \quad (13)$$

At steady state, we are: $\Delta i_{L_{pv}}\big|_{dis} \approx \Delta i_{L_{pv}}\big|_{ch}$
Capacitor current is given by:

$$i_{C_{pv}}\big|_{dis} = i_{pv} - i_{dc} \quad (14)$$

Thus, capacitor current ripple is: $\Delta v_{C_{pv}} = \frac{1}{C_{pv}} i_{C_{pv}} D_{dis} T_s$

**2.2.3. Validity of the modeling approach**

The state-space models are based on switched operating modes and used in an averaged framework. The validity relies on the assumption that the switching frequency is much higher than system dynamics ($f_{sw} \gg f_{systeme}$). Under this condition, state variables vary slowly compared to switching period and ripple remains small. This approximation is valid under: continuous conduction mode (CCM), high switching frequency relative to $L_{pv}$ and $C_{inv}$time constants, and negligible ripple. These assumptions justify the averaged model for control design.

with: $f_{sw} = \frac{1}{T_s}$ and $f_{systeme} = \frac{1}{2\pi\sqrt{L_{pv}C_{inv}}}$

**2.2.4. Determination of boosting factor and AC voltage gain**

To simplify the calculation of the BSSI gains, it is assumed that all voltage drops across the three-phase inverter switches, as well as those across the inductors, capacitors, and diodes, are negligible.

a. Boosting factor *B*

Simply, the boosting factor *B* is defined as the ratio of the DC-link voltage to the PV voltage:

$$B = \frac{u_{dc}}{u_{pv}}$$

Using the Volt-second balance defined by (10), we obtain:

$$B = \frac{1}{D_{dis}} = \frac{1}{1-D_{ch}} \quad (15)$$

b. AC gains relative

The AC voltage gain is defined as the ratio between the AC output voltage and the DC voltage supplied by the PV source. In this work, a conventional sinusoidal PWM modulation scheme is employed. We define $u_{ph}$ as the fundamental phase-to-neutral amplitude and $u_{LL}$ as the line-to-line RMS voltage are given by the following equations. The fundamental phase-to-neutral amplitude:

$$u_{ph} = m\frac{u_{dc}}{2} = m\frac{B.u_{PV}}{2\sqrt{2}} \quad (16)$$

Therefore, AC voltage gain between $u_{ph}\ and\ u_{pv}$ is given by:

$$G_{ph} = \frac{u_{dc}}{u_{PV}} = m\frac{B}{2\sqrt{2}} \quad (17)$$

The line-to-line RMS voltage:

$$u_{LL} = \sqrt{3}.m\frac{B.u_{PV}}{2\sqrt{2}} \quad (18)$$

Therefore, AC voltage gain between $u_{LL}\ and\ u_{pv}$ is given by:

$$G_{LL} = \sqrt{\frac{3}{2}}.m\frac{B}{2} \quad (19)$$

### 2.3. Induction motor model

The analysis and control of induction machines generally rely on their modeling in a rotating reference frame. This approach converts the original three-phase, time-varying quantities into steady or slowly varying variables, which greatly simplifies the study of the dynamic behavior as well as the design of control laws. In this work, the induction machine model is expressed in the flux-oriented $dq$ rotating reference frame. This formulation highlights the internal electromagnetic interactions and facilitates the separation between the active and reactive components [20]–[22]. The electrical dynamics of the induction motor are expressed as:

$$\begin{cases} \frac{di_{sd}}{dt} = -\frac{R}{\sigma L_s} i_{sd} + \omega_s i_{sq} + \frac{M}{\sigma L_s L_r}\left(\frac{1}{T_r}\varphi_{rd} + \omega\varphi_{rq}\right) \\ \qquad\qquad + \frac{1}{\sigma L_s} V_{sd} \\ \frac{di_{sq}}{dt} = -\frac{R}{\sigma L_s} i_{sq} - \omega_s i_{sd} + \frac{M}{\sigma L_s L_r}\left(\frac{1}{T_r}\varphi_{rq} - \omega\varphi_{rd}\right) \\ \qquad\qquad + \frac{1}{\sigma L_s} V_{sq} \\ \frac{d\varphi_{rd}}{dt} = \frac{M}{T_r} i_{sd} - \frac{1}{T_r}\varphi_{rd} + (\omega_s - \omega)\varphi_{rq} \\ \frac{d\varphi_{rq}}{dt} = \frac{M}{T_r} i_{sq} - \frac{1}{T_r}\varphi_{rq} - (\omega_s - \omega)\varphi_{rd} \end{cases} \quad (20)$$

where $= R_s + \frac{M^2}{L_r} R_r$ , $R = 1 - \frac{M^2}{L_r L_s}$ , $T_r = \frac{L_r}{R_r}$

The electromagnetic torque $T_e$ can be expressed as:

$$C_e = \frac{3}{2}\frac{pM}{L_r}\left(\varphi_{rd} i_{sq} - \varphi_{rq} i_{sd}\right) \quad (21)$$

Thus, the mechanical speed dynamics Ω of the machine can be expressed as:

$$\frac{d\Omega}{dt} = \frac{1}{J}(C_e - C_l + f\Omega) \quad (22)$$

## 3. ADAPTIVE VECTOR CONTROL OF IM-BSSI

Field-oriented control (FOC) remains a benchmark technique for high-performance control of induction machines, owing to its capability to achieve an effective decoupling between flux and torque components. Nevertheless, its direct application to integrated energy conversion systems such as the induction motor–BSSI is not straightforward. In such configurations, the presence of strong nonlinearities, coupling effects, and converter-induced constraints significantly degrades the performance of conventional FOC schemes, particularly under parameter uncertainties and external disturbances. To overcome these limitations, an adaptive vector control framework is proposed. The core idea consists in redefining the control input by incorporating a hybrid control structure that synergistically combines two advanced control strategies. First, a SMC law is employed to regulate the DC-link voltage, ensuring robustness against disturbances and model uncertainties. Second, the speed control loop is governed by an adaptive PI controller designed using Lie derivative-based feedback linearization, allowing for an explicit compensation of system nonlinearities and an online adjustment of controller gains. The complete structure of the proposed adaptive vector control scheme is depicted in Figure 9. Where the interaction between the inner current loops, the DC-link regulation, and the adaptive speed control loop is clearly illustrated.

### 3.1. SMC of DC-bus voltage

By combining systems (7) and (12), the complete DC-link voltage model is obtained:

$$\dot{x} = Ax + Bu \quad (23)$$

with $A = (1 - D_{ch})A_{dis}$ and $B = D_{ch}B_{ch} + (1 - D_{ch})B_{dis}$

Therefore, the state-space model can be written as:

$$\frac{d}{dt}\begin{bmatrix} i_{L_{pv}} \\ u_{dc} \end{bmatrix} = \begin{bmatrix} 0 & \frac{-(1-D_{ch})}{L_{pv}} \\ 0 & 1 \end{bmatrix}\begin{bmatrix} i_{L_{pv}} \\ u_{dc} \end{bmatrix} + \begin{bmatrix} \frac{1}{L_{pv}} & 0 \\ 0 & \left(D_{ch}\left(C_{pv}+\frac{1}{C_{inv}}\right)-C_{pv}\right) \end{bmatrix}\begin{bmatrix} u_{pv} \\ i_{dc} \end{bmatrix} \quad (24)$$

The output vector is given by: $y(t) = [0 \quad 1]\begin{bmatrix} i_{L_{pv}} \\ u_{dc} \end{bmatrix}$

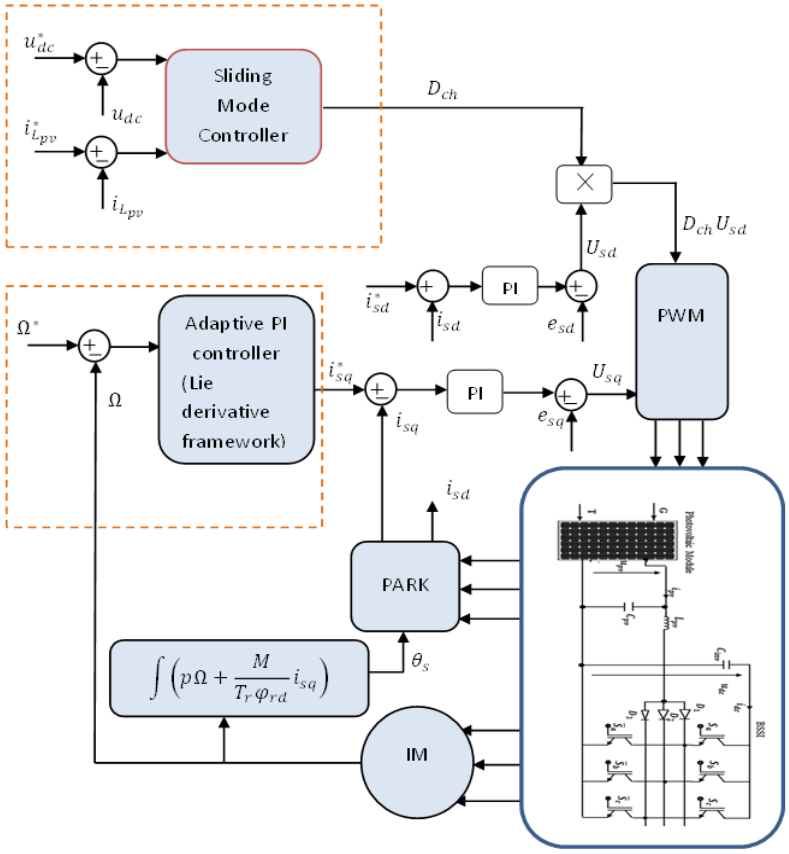



Figure 9. Proposed adaptive vector control scheme for the IM–BSSI system integrating sliding mode DC-link regulation and adaptive PI speed control based on feedback linearization

The state-space model in (24) represents the model of one phase of three phases BSSI. The SMC is based on defining a sliding surface S and designing a control law that forces the system to remain on this surface. From model (24), the state errors are defined as:

$$\begin{cases} e_1 = i_{L_{pv}} - i^*_{L_{pv}} \\ e_2 = u_{dc} - u^*_{dc} \end{cases} \quad (25)$$

To guarantee the asymptotic convergence of the error dynamics to the origin, an appropriate sliding surface for the DC-link is defined as:

$$S = \lambda_1 e_1 + \lambda_2 e_2 \quad (26)$$

where $\lambda_1$ , $\lambda_2$ are the positive weighting coefficients.

After substituting the analytical forms of $e_1$ and $e_2$, the sliding surface can be reformulated as follows in vector notation:

$$S = C^T x - r(t) \quad (27)$$

where: $C^T = [\lambda_1 \ \lambda_2]$ , $r(t) = \lambda_1 i^*_{L_{pv}} + \lambda_2 u^*_{dc}$, $x = [i_{L_{pv}} \quad u_{dc}]^T$

By differentiating, we obtain:

$$\dot{S} = C^T \dot{x} - \dot{r}(t) = C^T (AD_{ch} x + BD_{ch} u) - \dot{r}(t) \quad (28)$$

Hence, $\dot{S} = \lambda_1 \left( -\frac{-(1-D_{ch})}{L_{pv}} u_{dc} \right) + \lambda_2 u_{dc} + \lambda_1 \frac{1}{L_{pv}} u_{pv} + \lambda_2 \left( D_{ch} \left( C_{pv} + \frac{1}{C_{inv}} \right) - C_{pv} \right) i_{dc} - \dot{r}(t)$

By rearranging the above expression, we obtain:

$$\dot{S} = a(x,u) + b(x,u) D_{ch} - \dot{r}(t) \quad (29)$$

where:

$$a(x,u) = -\lambda_1 \frac{1}{L_{pv}} u_{dc} + \lambda_2 u_{dc} + \lambda_1 \frac{1}{L_{pv}} u_{pv} - \lambda_2 C_{pv} i_{dc}$$
$$b(x,u) = \lambda_1 \frac{1}{L_{pv}} u_{dc} + \lambda_2 \left( C_{pv} + \frac{1}{C_{inv}} \right) i_{dc}$$

The objective is to drive the surface dynamics toward zero, i.e. $\dot{S} = 0$. To achieve this goal, solving (29) yields the equivalent control law:

$$D_{cheq} = \frac{\dot{r}(t) - a(x,u)}{b(x,u)} \quad (30)$$

Since the control strategy is based on sliding mode theory, a switching term $ksign(S)$ is added to ensure that the system trajectories remain on the sliding surface, and the control law (30) becomes:

$$D_{ch} = \frac{\dot{r}(t) - a(x,u)}{b(x,u)} - ksign(S) \quad (31)$$

The proposed control law $U_d$ in proposed FOC of IM-BSSI can be expressed as follows:

$$U_d = D_{ch} U_{sd} \quad (32)$$

where $U_{sd}$is the direct-axis voltage command generated by the conventional FOC scheme, and $D_{ch}$is the shoot-through duty cycle produced by the SMC of the BSSI converter.

The multiplication by $D_{ch}$ allows the direct-axis control signal to be dynamically adjusted according to the operating conditions of the DC–DC conversion stage. This formulation reflects the interaction between the motor drive and the photovoltaic power-conditioning system. While the FOC algorithm determines the voltage reference required to regulate the rotor flux and ensure decoupled control of the induction motor, the SMC-based BSSI controller regulates the converter operation and the DC-link voltage through the shoot-through duty cycle. Consequently, the resulting control signal $U_d$combines the advantages of both control strategies, preserving the dynamic performance of the vector control while enhancing system robustness against irradiance variations, parameter uncertainties, and load disturbances. Therefore, the (32) represents an adaptive correction of the conventional FOC voltage command by the SMC-generated duty cycle, ensuring coordinated operation between the induction motor drive and the BSSI converter.

### 3.1.1. Stability analysis

The stability of the SMC system is investigated using a suitable Lyapunov function. By considering the candidate function:

$$V = \frac{1}{2} S^2 \quad (33)$$

The stability condition is satisfied if its time derivative fulfills:

$$\dot{V} = S\dot{S} = S(a(x,u) + b(x,u) \left( \frac{\dot{r}(t) - a(x,u)}{b(x,u)} - ksign(S) \right) - \dot{r}(t)) < 0 \quad (34)$$

After calculation, we obtain:

$$\dot{V} = -K.b(x,u).S.sign(S) \quad (35)$$

For any strictly positive control gain $K$, the evaluated expression (36) remains strictly negative. Consequently, the Lyapunov stability condition is satisfied, which guarantees that the selected sliding surface is asymptotically stable.

### 3.2. Speed control by adaptive PI controller

To ensure high-performance speed regulation under nonlinear operating conditions, an adaptive proportional–integral (PI) control strategy grounded in the Lie derivative framework is developed. The proposed approach leverages input–output feedback linearization to reshape the inherently nonlinear dynamics into a tractable quasi-linear representation, thereby facilitating systematic controller synthesis. In this context, the control input $u(t)$ is decomposed into a model-based compensation term and an adaptive PI correction component, expressed as:

$$u(t) = u_M(t) + K_p e + K_i \int_{t_0}^{t} e\, dt \tag{36}$$

The feedforward term $u_M(t)$, derived from the nonlinear model, is given by:

$$u_M(t) = \frac{-\sum_{j=0}^{r} n_j L_f^j h}{n_r L_g L_f^{r-1} h} \tag{37}$$

where $L_f^j h$ and $L_f^{r-1} h$ denote successive Lie derivatives of the output function, and $n_j$ $(j = 0 \ldots r)$ are constant design coefficients ensuring appropriate dynamic shaping. This term effectively cancels the dominant nonlinearities and enforces a desired input–output behavior [23]. To enhance robustness against parameter uncertainties and external disturbances, the PI gains are not fixed but dynamically adapted online according to the instantaneous tracking error $e = (x_{ref} - x)$, defined as the deviation between the reference and actual motor speeds. The overall architecture of the proposed speed control scheme is depicted in Figure 10.

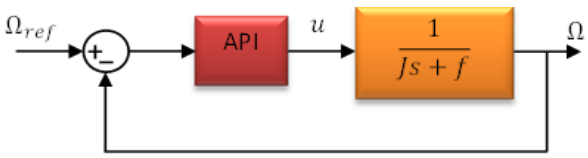



Figure 10. Speed control scheme

#### 3.2.1. API modeling

The considered mechanical subsystem is described by:

$$\frac{d\Omega}{dt} = \frac{f}{J}\Omega + \frac{1}{J}(C_e - C_l) \tag{38}$$

The system can be rewritten in the standard nonlinear state-space form:

$$\dot{x} = f(x) + g(x).u \text{ and } y = \Omega = h(x)$$

where $x = \Omega$ denotes the state variable, with: $g(x) = \frac{1}{J}$ and $f(x) = \frac{f}{J}\Omega - \frac{1}{J}C_l$

#### 3.2.2. Feedback linearization and control law

In this case, the system exhibits a relative degree $r = 1$, leading to:

$$\dot{\Omega} = L_f h(x) + L_g h(x) u \tag{39}$$

where $L_f h(x) = \frac{\partial h}{\partial x} f(x) = \frac{f}{J}\Omega - \frac{1}{J}C_l$, $L_g h(x) = \frac{\partial h}{\partial x} g(x) = \frac{1}{J}$

Thus, the system dynamics become:

$$\dot{\Omega} = \left(\frac{f}{J}\Omega - \frac{1}{J}C_l\right) + \frac{1}{J}u \tag{40}$$

By selecting the control law:

$$u = J\left(v - L_f h(x)\right) \tag{41}$$

The closed-loop system reduces to a fully linear form:

$$\dot{\Omega} = v \tag{42}$$

To achieve the desired tracking performance, the auxiliary control input $v$ is chosen as:

$$v = \dot{\Omega}_{ref} + K_p e + K_i \int_{t_0}^{t} e\, dt \tag{43}$$

Consequently, the overall control law is obtained as:

$$u = \left[J\dot{\Omega}\text{ref} + K_p J e + J K_i \int_{t_0}^{t} e\, dt - (f\Omega - C_l)\right] \tag{44}$$

**3.2.3. Adaptive gain design via Lyapunov stability**

The error dynamics can be written as:

$\dot{e} = \dot{\Omega}_{ref} - \dot{\Omega} = -K_p e - K_i \int_{t_0}^{t} e\, dt$

Let: $= \int_{t_0}^{t} e\, dt$ , yielding:

$$\begin{cases} \dot{e} = -K_p e - K_i x \\ \dot{x} = e \end{cases} \tag{45}$$

To ensure closed-loop stability, the following Lyapunov candidate function is considered:

$$V = \frac{1}{2}e^2 + \frac{1}{2}x^2 + \frac{1}{2\lambda_p}\left(K_p - K_{p0}\right)^2 + \frac{1}{2\lambda_i}(K_i - K_{i0})^2 \tag{46}$$

where $\lambda_p$ and $\lambda_i$ are positive adaptation gains, $K_{p0}$ and $K_{i0}$ are unknown initial parameters. The time derivative of (46) leads to:

$$\dot{V} = -K_p e^2 - K_i ex + ex + \frac{1}{\lambda_p}\dot{K}_p\left(K_p - K_{pref}\right) + \frac{1}{\lambda_i}\dot{K}_i\left(K_i - K_{iref}\right) \tag{47}$$

By selecting the following adaptation laws:

$$\begin{cases} \dot{K}_p = \lambda_p e^2 \\ \dot{K}_i = \lambda_i x.e \end{cases} \tag{48}$$

$$K_p = \lambda_p \int e^2 dt \tag{49}$$

$$K_i = \lambda_i \int x.e dt \tag{50}$$

The Lyapunov derivative simplifies to: $\dot{V} = -K_p e^2 \leq 0$

Thus, the stability of the error dynamics is guaranteed in the sense of Lyapunov. Prior to adaptation, the initial gains are selected based on the desired closed-loop dynamics: $K_{p0} = \frac{2\xi\omega_n - L_f}{L_g}$ and $K_{i0} = \frac{\omega_n^2}{L_g}$ , where: $\omega_n$ is the desired natural frequency, $\xi$ is the damping ratio.

To prevent parameter drift and ensure boundedness of the adaptive gains, saturation functions are introduced. Finally, the adaptive gains are updated as:

$$K_p = K_{p0} + \lambda_p \int e^2 dt + sat(K_p) \tag{51}$$

$$K_i = K_{i0} + \lambda_i \int x e dt + sat(K_i) \tag{52}$$

The overall structure of the proposed adaptive controller is illustrated in Figure 11.

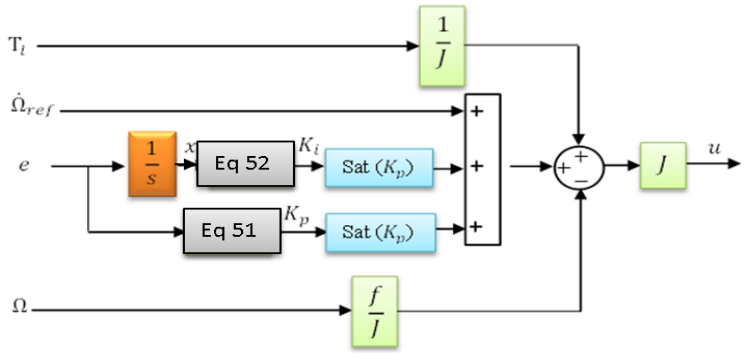



Figure 11. Structure of the proposed adaptive controller

### 3.2.4. Controller parameter tuning procedure

To achieve satisfactory performance of the proposed control strategy for a photovoltaic (PV)-fed induction motor using a BSSI. An appropriate selection of the SMC and API controller parameters is essential. Since the overall system exhibits nonlinear dynamics and strong coupling between control loops, an analytical tuning approach alone is not sufficient. Therefore, a heuristic, simulation-based tuning procedure is employed to systematically adjust the controller gains in order to ensure stability, fast dynamic response, and robust operation under varying conditions. The corresponding tuning procedure is summarized in the Figure 12.

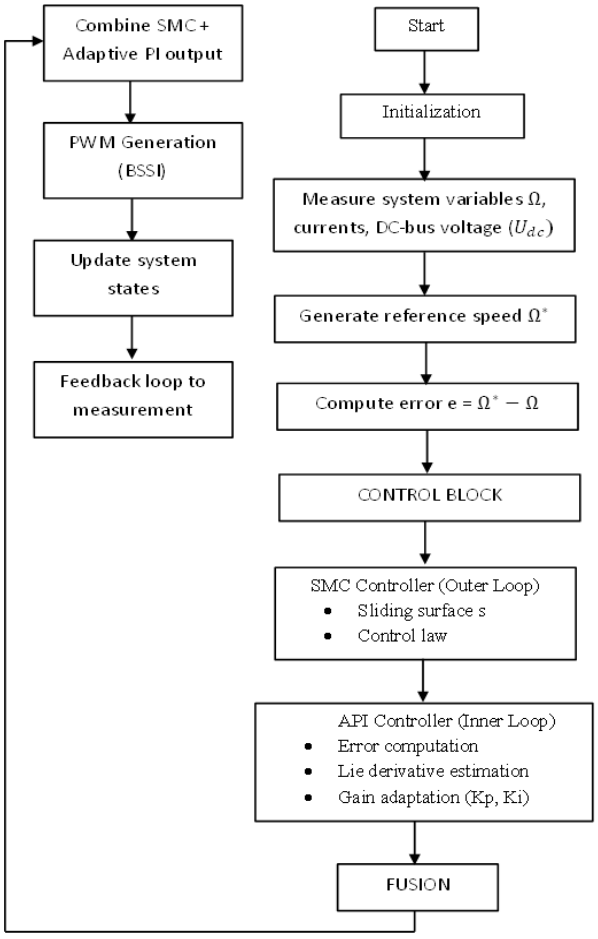



Figure 12. Flowchart of corresponding tuning procedure

## 4. PROTECTION SYSTEM

The protection scheme is implemented using two hysteresis relays **(**relay 1 and relay 2), in Figure 13. These relays are responsible for generating the control signals applied to the power switches S1 and S2, respectively, thereby ensuring reliable supervision of the system operating conditions [24]. The relay-3 is designed to activate the dissipative resistor connected to the DC-bus when the bus voltage $u_{dc-max} = 480V$ exceeds the maximum threshold specified by the IM-BSSI system. This operating condition corresponds to an excess of energy supplied by the panel. Conversely, when the DC-bus voltage falls below the predefined lower threshold of $u_{dc-min} = 350V$, the dissipative resistor is automatically disconnected, contributing to effective DC-bus voltage regulation and system stability. The relay_4 provides an additional safety mechanism by disconnecting the IM-BSSI system from the DC-bus in the event of critical faults, such as short circuits occurring within the BSSI**,** the motor, or other abnormalities that may adversely affect system performance. This protective action prevents potential damage to key components, particularly the panel and the DC–DC boost converter, and ensures safe and robust operation of the overall system. The flowchart presented in Figure 14 provides a visual representation of the decision-making procedure for controlling the activation and deactivation of the dissipative resistor (S1) and the load (S2). The control logic is based on the measured bus voltage and current, incorporating a hysteresis mechanism to ensure reliable protection of the system.

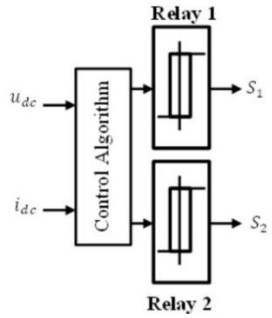



Figure 13. Protection system

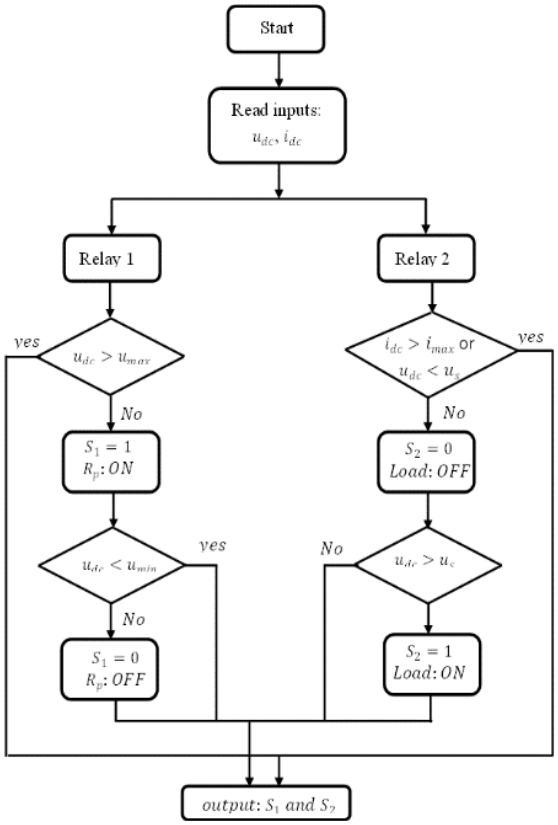



Figure 14. Flowchart: DC-bus protection system for IM-BSSI using hysteresis relays

## 5. SIMULATION AND EXPERIMENTAL RESULTS

Recent works have demonstrated the effectiveness of adaptive PI and intelligent control strategies in PV systems under uncertain conditions [25]–[28]. These results support the robustness of the proposed API-based method presented in this study. The performance of the proposed control strategy for the PV-fed IM–BSSI system is assessed through both simulation studies and experimental investigations. Initially, numerical simulations are carried out using MATLAB/Simulink to evaluate the feasibility and to analyze the dynamic behavior of the overall system. Subsequently, experimental tests are performed on the developed test bench in order to validate the practical implementation of the proposed approach and to demonstrate its real-time applicability. Figure 15 depicts the experimental setup implemented at the LTI Laboratory (Laboratoire des Technologies Innovantes, EA 3899), Institute of Technology, University of Soissons, France, which is recognized for its expertise in control and energy systems integration. The test bench mainly consists of a 3 kW photovoltaic (PV) generator used as the primary energy source, along with voltage and current sensors for measuring electrical variables at different points of the system, with real-time visualization via an oscilloscope. In addition, the setup includes a 1.5 kW induction motor, completing the experimental platform for system validation.

The electrical parameters of the induction motor adopted in the simulations are $R_s = 5.72\Omega$ , $R_r = 4.2\Omega$ , $L_s = 0.462H$ , $L_r = 0.462H$, $M = 0.4402H$, J= $0.0049Kg.m^2$, $f = 0.001\,N.m.s/rad$. Figure 16 illustrates the experimental result of the total harmonic distortion (THD) analysis demonstrates the effectiveness of the proposed control approach for the photovoltaic-powered IM–BSSI system. The conventional PI regulator exhibits pronounced THD peaks, mainly due to its fixed parameter structure, which is inadequate for handling the system's transient dynamics. In contrast, the adaptive PI controller significantly mitigates harmonic distortion by continuously tuning its gains in response to operating conditions. This adaptive behavior enables a smoother dynamic response and limits the generation of harmonic components. Consequently, the proposed hybrid control scheme achieves a substantial reduction in THD while enhancing the quality of the stator currents in both transient and steady-state regimes.

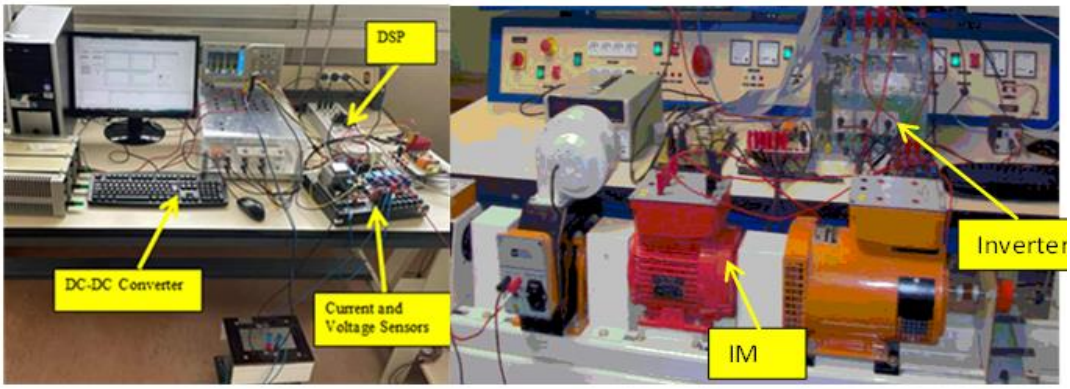



Figure 15. Experimental test bench in the LTI Laboratory

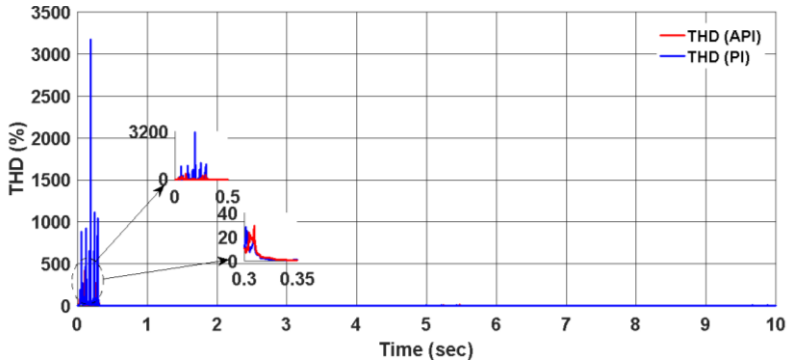



Figure 16. Temporal evolution of the THD

The profiles illustrated in Figures 17 and 18 represent the temporal evolution of solar irradiance and temperature, respectively, and are considered solely within the simulation test. The irradiance exhibits rapid transitions [1000 800 500 1000 800] W/m², while the temperature rises from 25°C to 50°C before decreasing to nearly 5°C. Such pronounced variations are intentionally introduced to emulate harsh environmental conditions and to rigorously assess the robustness of the proposed control strategy.

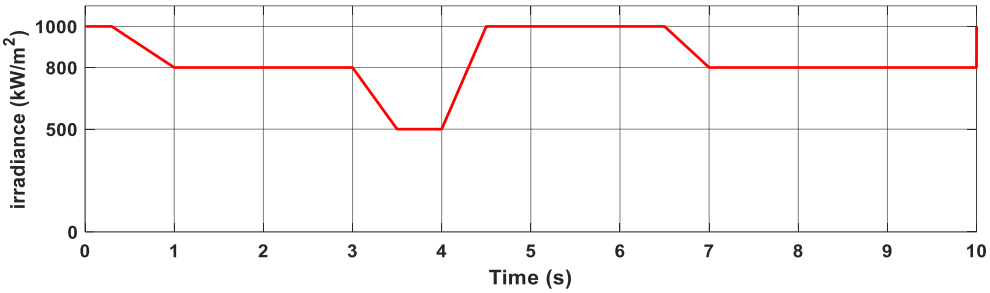



Figure 17. Variations in irradiance G

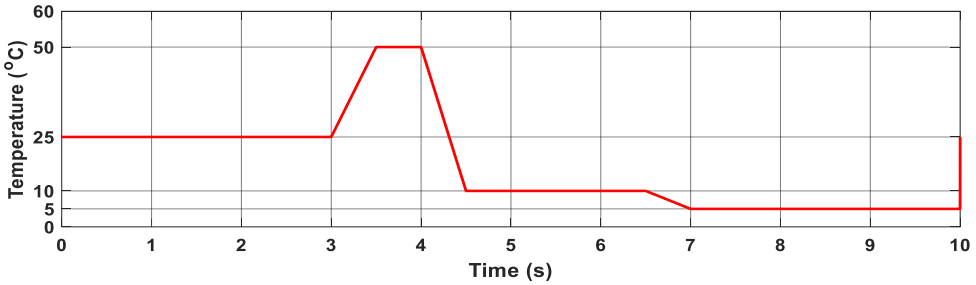



Figure 18. Variations in temperature

Figures 19 and 20 show the speed response from simulations and experiments. The classical PI controller exhibits significant overshoot, oscillations, and slow settling due to its fixed gains being unsuitable for the nonlinear IM–BSSI dynamics. In contrast, the adaptive PI (based on the Lie derivative) achieves faster tracking with reduced overshoot and better damping. This performance gap is more pronounced experimentally, where noise, parametric uncertainties, and unmodeled dynamics exacerbate oscillations in the classical PI. The application of a load at t = 2 s highlights the adaptive PI's robustness: it maintains a smoother response and quickly restores reference speed, whereas the classical PI experiences large fluctuations. The SMC of the DC-bus further enhances performance by managing current demands during nonlinear transients. The proposed strategy thus ensures stable, high-performance operation in both simulation and real conditions.

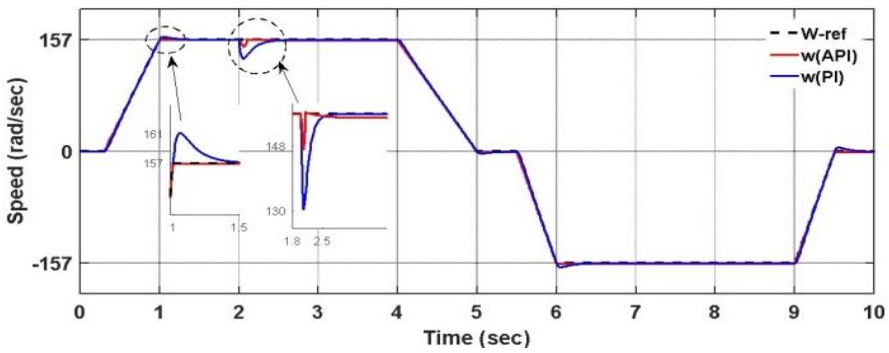



Figure 19. Speed characteristic (simulation)

Figures 21 and 22 illustrate the electromagnetic torque response under both simulation and experimental conditions. During the intervals t = [0.3–1 s], [4–5 s], [5.5–6 s], and [9–9.5 s], non-zero torque values are observed even at no load, mainly due to friction effects and transient acceleration/deceleration phases. In both cases, the conventional PI controller exhibits slower disturbance rejection compared to the adaptive PI strategy. This results in more pronounced deviations and longer recovery times. In contrast, the adaptive PI ensures faster compensation and smoother torque behavior, thereby demonstrating improved robustness and superior dynamic performance.

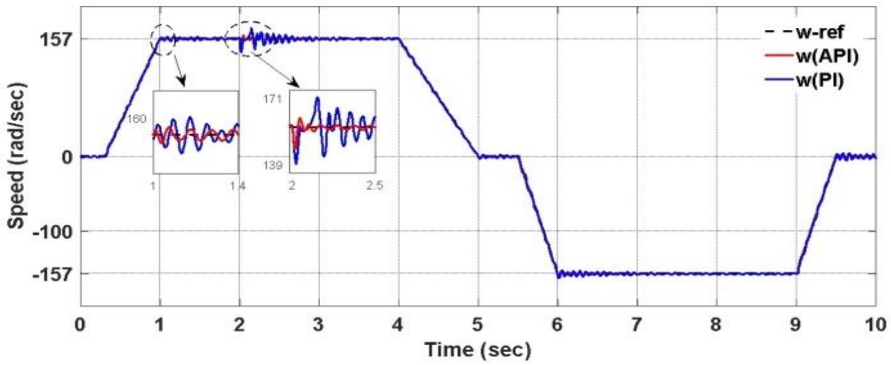



Figure 20. Speed characteristic (experimental)

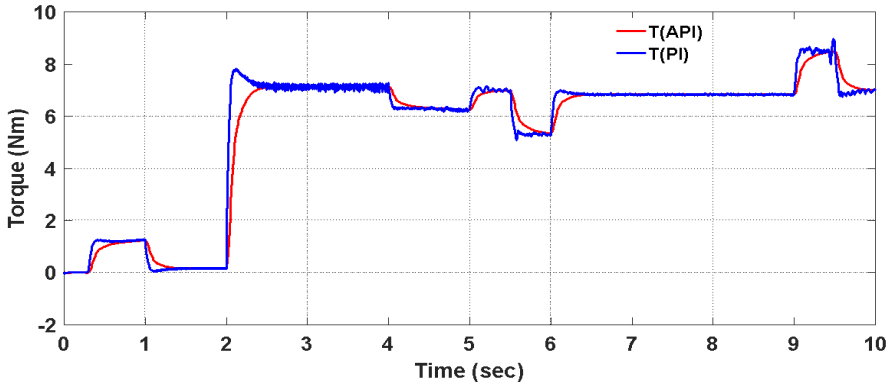



Figure 21. Torque characteristic

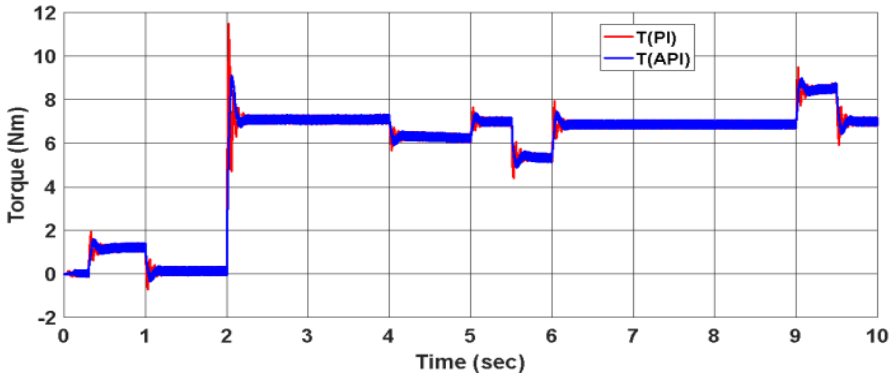



Figure 22. Torque characteristic (experimental)

Figures 23 and 24 respectively present the evolution of the DC-bus voltage $u_{dc}$ under simulation and experimental conditions. In the simulation results, the dynamic behavior of $u_{dc}$ accurately reflects the

influence of temperature and solar irradiance variations applied at the input of the photovoltaic generator, thereby highlighting the system sensitivity to environmental disturbances. In contrast, during experimental tests, the DC-bus voltage remains nearly constant, which can be attributed to the absence of variations in environmental conditions, particularly temperature and irradiance levels, which are maintained stable throughout the experiments.

Furthermore, Figures 25 and 26 depict the profiles of the photovoltaic voltage $u_{PV}$ in both cases. A clear amplification of the PV voltage can be observed, demonstrating the effective operation of the boost converter (180 to 540V). This result confirms the capability of the system to step up the voltage level and validates the feasibility and effectiveness of the proposed hybrid control strategy for the PV–IM–Boost system.

Regarding the omission of a dedicated MPPT algorithm, it is important to note that conventional PV-fed systems rely on MPPT to maximize energy extraction under varying atmospheric conditions. However, this typically increases control complexity, computational requirements, and system cost, and is often associated with multi-stage power conversion architectures that may reduce overall reliability. In the proposed configuration, the MPPT stage is intentionally removed and replaced by a direct control of the BSSI structure. This design choice prioritizes simplicity, robustness, and fast dynamic response rather than strict maximization of instantaneous PV power.

Although the absence of MPPT may lead to a reduction in harvested energy under rapidly changing irradiance conditions, the proposed approach offers a favorable trade-off by reducing the number of control loops, simplifying implementation, and improving system reliability. Consequently, the presented results highlight that the system maintains stable operation and satisfactory voltage boosting performance while operating with a simplified control structure, which constitutes a key design objective of this work.

Figures 27 and 28 present the simulated and experimental stator currents, respectively. Specifically, Figures 27(a) and 27(b) show the simulated stator currents $i_{s\alpha}$ and $i_{s\beta}$, whereas Figures 28(a) and 28(b) present the corresponding experimental stator currents. The results indicate that the conventional PI controller yields higher current amplitudes than the adaptive PI (API) strategy, reflecting increased electrical stress under classical regulation. In the experimental case, residual chattering is observed, primarily caused by sensor measurement noise, acquisition imperfections, and external disturbances.

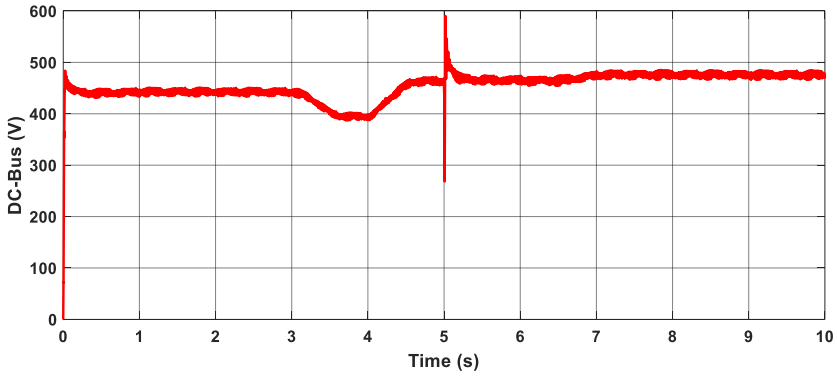



Figure 23. DC-bus voltage $u_{dc}$(simulation)

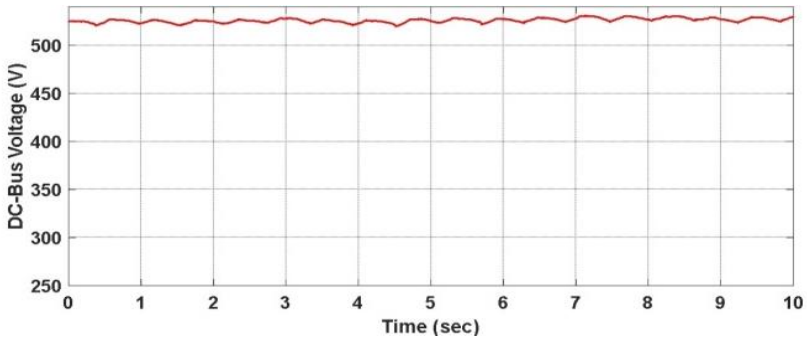



Figure 24. DC-bus voltage $u_{dc}$(Experimental)

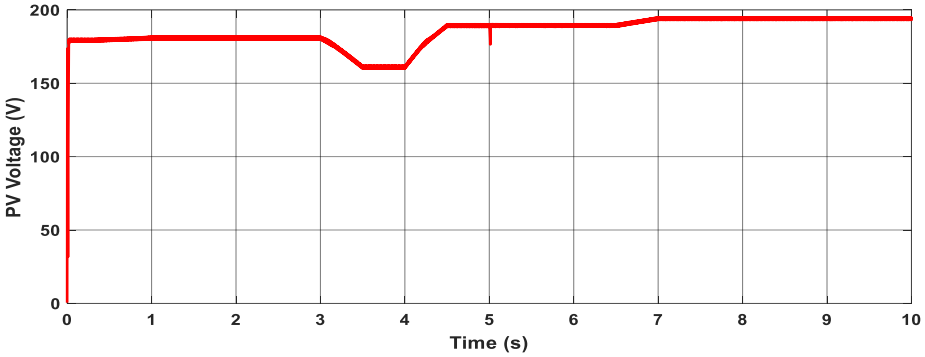



Figure 25. PV voltage $u_{PV}$(simulation)

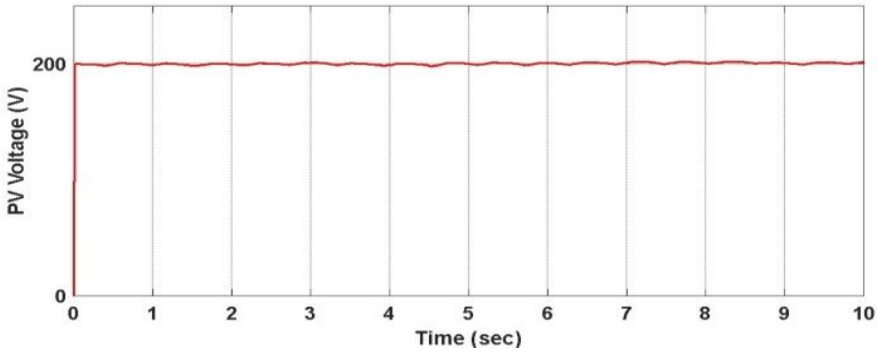
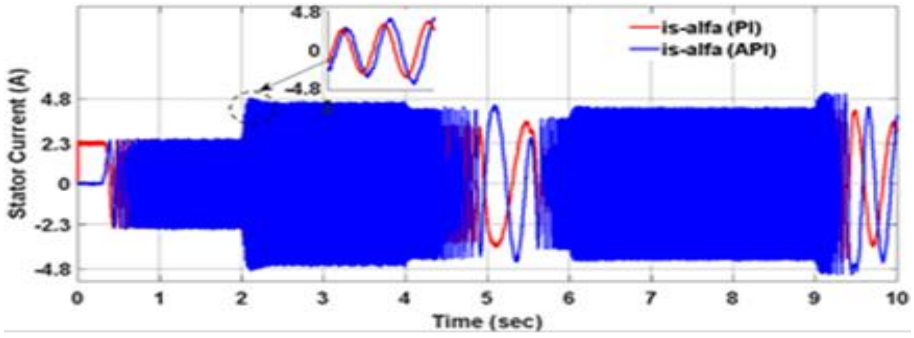
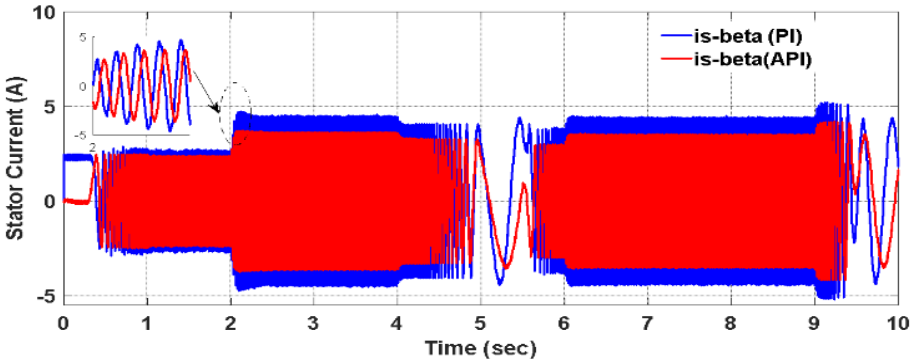



Figure 26. PV voltage $u_{PV}$(experimental)

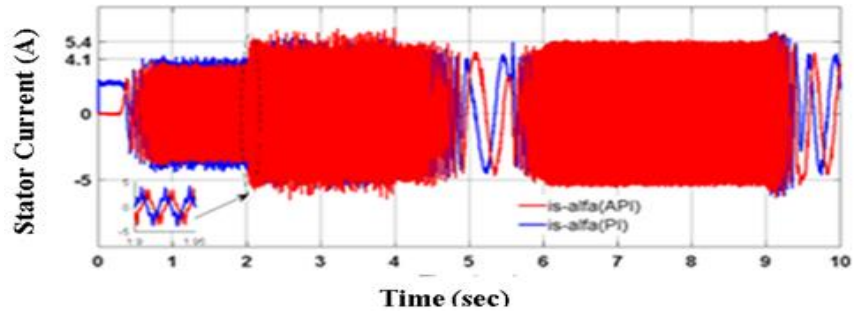



(a)

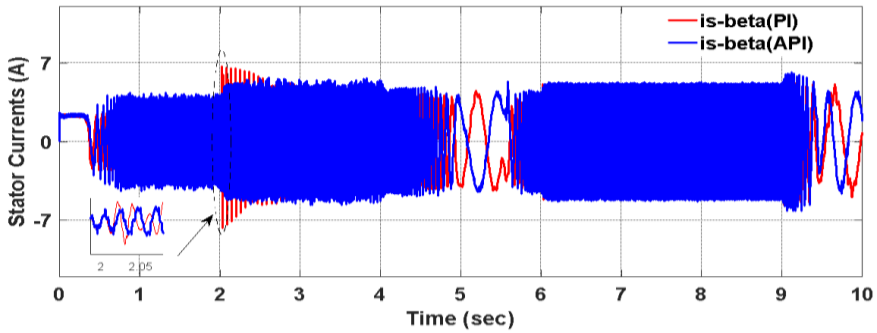



(b)

Figure 27. Simulated stator currents: (a) $i_{s\alpha}$ and (b) $i_{s\beta}$




(a)




(b)

Figure 28. Experimental stator current: (a) $i_{s\alpha}$ and (b) $i_{s\beta}$

To objectively evaluate the effectiveness of the proposed Adaptive PI (API) controller, a quantitative comparison with the conventional PI controller is presented in Table 3. The comparison includes key dynamic and steady-state performance indicators, namely rise time, settling time, overshoot, steady-state error, and THD. The obtained results demonstrate that the proposed API controller significantly enhances the overall performance of the IM–BSSI drive system. Although both controllers exhibit comparable rise times, the API controller reduces the average settling time from 1.087 s to 0.938 s, corresponding to an improvement of 13.7%. Furthermore, the overshoot is drastically reduced from 2.90% to 0.42%, representing an 85.5% improvement and confirming the superior damping capability of the proposed approach. The steady-state error remains negligible for both controllers, while the API ensures more accurate speed tracking under successive speed reversals and operating condition changes. In addition, the harmonic analysis reveals that the proposed API controller reduces the current THD from 4.82% to 2.67%, yielding a harmonic reduction of 44.6%. These results clearly demonstrate that the proposed API controller provides better transient response, enhanced tracking accuracy, and improved power quality compared with the conventional PI controller, thereby validating its suitability for high-performance induction motor drive applications powered by the BSSI system.

Table 3. Quantitative performance comparison between the conventional PI and the proposed adaptive PI (API) controllers

| Performance index | Classical PI | Proposed API | Improvement (%) |
|---|---|---|---|
| Rise time (s) | 0.524 | 0.540 | −3.1 % |
| Settling time (s) | 1.087 | 0.938 | 13.7 % |
| Overshoot (%) | 2.90 | 0.42 | 85.5 % |
| Steady-state error (rad/s) | 0.11 | 0.10 | 9.1 % |
| THD (%) | 4.82 | 2.67 | 44.6 % |

## 6. CONCLUSION

This paper has presented an adaptive control strategy for a PV-fed induction motor drive system based on a BSSI system. The proposed control strategy, combining SMC with a Lie-derivative-based adaptive PI regulator, has demonstrated high reliability and effectiveness through both simulation and experimental results. The proposed approach ensures accurate speed tracking, strong disturbance rejection capability, improved dynamic response, and enhanced voltage boosting performance of the PV-fed IM–BSSI

system without requiring a conventional MPPT stage. Consequently, the proposed topology contributes to simplifying the overall control architecture while reducing system complexity and conversion stages. The main contribution of this work lies in the integration of the BSSI system with vector control of the induction motor using a hybrid SMC–API scheme without MPPT, providing a simplified yet efficient control structure suitable for renewable energy applications. In addition, the integration of the robustness of SMC with the adaptability of the adaptive PI controller significantly improves system stability, transient performance, and control accuracy compared with conventional vector control techniques (FOC). Quantitative performance analysis confirmed reduced overshoot, fast settling time, improved efficiency, and lower harmonic distortion, highlighting the superiority of the proposed strategy.

From an application perspective, the proposed system is particularly suitable for photovoltaic-based installations such as solar water pumping systems, where reliable speed regulation is required under fluctuating irradiance conditions. In addition, it can be extended to industrial drive applications including pumps, fans, and conveyor systems operating under variable load conditions.

Regarding scalability, the modular structure of the BSSI system allows straightforward extension to higher power levels through appropriate design of semiconductor devices and passive components. Furthermore, the control strategy can be generalized to multi-machine or multi-phase configurations with minimal modifications, making it suitable for medium- and large-scale renewable energy systems.

Finally, the elimination of MPPT reduces system complexity and computational burden, which enhances real-time implementation capability and makes the proposed approach attractive for low-cost embedded renewable energy applications.

## REFERENCES


[1] Fang Zheng Peng, "Z-source inverter," *IEEE Transactions on Industry Applications*, vol. 39, no. 2, pp. 504–510, Mar. 2003, doi: 10.1109/TIA.2003.808920.

[2] S. S. Lee and Y. E. Heng, "Improved single-phase split-source inverter with hybrid quasi-sinusoidal and constant PWM," *IEEE Transactions on Industrial Electronics*, vol. 64, no. 3, pp. 2024–2031, 2017, doi: 10.1109/TIE.2016.2624724.

[3] C. Yin, Z. Xin, W. Ding, and P. C. Loh, "Modified split-source inverter with single-phase dual power decoupling," *IET Power Electronics*, vol. 13, no. 11, pp. 2201–2211, 2020, doi: 10.1049/iet-pel.2020.0013.

[4] A. A. Abd-Elaziz, S. M. Dabour, M. F. Elmorshedy, and E. M. Rashad, "Application of FCS-MPC for split-source inverter-based single-phase grid-connected PV systems," in *2023 IEEE Conference on Power Electronics and Renewable Energy (CPERE)*, IEEE, Feb. 2023, pp. 1–6. doi: 10.1109/CPERE56564.2023.10119629.

[5] A. Kumar and P. Sensarma, "Operating modes based review of single-stage buck-boost inverters," *IECON Proceedings (Industrial Electronics Conference)*, vol. 2019-Octob, pp. 1904–1909, 2019, doi: 10.1109/IECON.2019.8927563.

[6] P. B. Miyani, A. V. Sant, G. Sharma, P. N. Bokoro, and R. Kumar, "Quasi-Z source inverter based 3-phase grid-tied photovoltaic system with dual loop shoot-through control using discrete time sliding mode control," *Scientific African*, vol. 29, p. e02936, Sep. 2025, doi: 10.1016/j.sciaf.2025.e02936.

[7] J. de Azevedo Borges and F. B. Grigoletto, "Finite set model predictive control of grid connected split-source inverters," in *2017 Brazilian Power Electronics Conference (COBEP)*, IEEE, Nov. 2017, pp. 1–6. doi: 10.1109/COBEP.2017.8257297.

[8] S. M. Dabour *et al.*, "Modeling and control of single-stage quadratic-boost split-source inverters," *IEEE Access*, vol. 10, pp. 24162–24180, 2022, doi: 10.1109/ACCESS.2022.3153510.

[9] O. N. Mahmmoud, S. R. Mehdi, K. S. Gaeid, and A. L. S. Al-Tameemi, "Solar cell split source inverter for induction motor with computer control," *International Journal of Power Electronics and Drive Systems*, vol. 14, no. 1, pp. 174–184, 2023, doi: 10.11591/ijpeds.v14.i1.pp174-184.

[10] A. Sabrié, A. Battiston, J. Y. Gauthier, and X. Lin-Shi, "Three-phase bidirectional active split source inverter for automotive traction application," *Mathematics and Computers in Simulation*, vol. 224, pp. 96–118, 2024, doi: 10.1016/j.matcom.2023.08.045.

[11] S. M. Dabour, A. A. Aboushady, M. A. Elgenedy, I. A. Gowaid, and M. E. Farrag, "A vector control strategy for five-phase drives fed by simplified split-source inverters," in *2023 IEEE Conference on Power Electronics and Renewable Energy (CPERE)*, IEEE, Feb. 2023, pp. 1–6. doi: 10.1109/CPERE56564.2023.10119603.

[12] M. Wageh, S. M. Dabour, and R. M. Mostafa, "A new four-switch split-source boosting inverter: Analysis and modulation," in *2022 23rd International Middle East Power Systems Conference (MEPCON)*, IEEE, Dec. 2022, pp. 1–7. doi: 10.1109/MEPCON55441.2022.10021772.

[13] S. Ibrahim, S. A. Hamad, A. S. Mansour, M. S. Zaky, A.-G. A. Abdel-Samei, and M. W. Lotfy, "Power efficiency enhancement in high-boost three-phase split-source inverters," *Engineering, Technology & Applied Science Research*, vol. 15, no. 3, pp. 22983–22989, Jun. 2025, doi: 10.48084/etasr.10670.

[14] Y. S. Abdulhussein and A. Gün, "Design and implementation of a three-phase buck-boost split-source inverter (BSSI)," *Electronics*, vol. 15, no. 4, p. 808, Feb. 2026, doi: 10.3390/electronics15040808.

[15] L. Monjo, L. Sainz, J. J. Mesas, and J. Pedra, "Quasi-Z-source inverter-based photovoltaic power system modeling for grid stability studies," *Energies*, vol. 14, no. 2, p. 508, Jan. 2021, doi: 10.3390/en14020508.

[16] A. A. Abd-Elaziz, S. M. Dabour, M. F. Elmorshedy, and E. M. Rashad, "Modeling and control of stand-alone photovoltaic system based on split-source inverter," in *2021 22nd International Middle East Power Systems Conference (MEPCON)*, IEEE, Dec. 2021, pp. 469–476. doi: 10.1109/MEPCON50283.2021.9686249.

[17] M. W. Lotfy, S. M. Dabour, R. M. Mostafa, D. J. Almakhles, and M. F. Elmorshedy, "Modeling and control of a voltage-lift cell split-source inverter with MPPT for photovoltaic systems," *IEEE Access*, vol. 11, pp. 54699–54712, 2023, doi: 10.1109/ACCESS.2023.3280602.

[18] C. Pica, R. Munteanu, S. Pavel, and H. Beleiu, "Modeling of photovoltaic panels," in *2018 International Conference and Exposition on Electrical And Power Engineering (EPE)*, IEEE, Oct. 2018, pp. 0769–0773. doi: 10.1109/ICEPE.2018.8559884.

[19] H. Romaissa, Y. Beddiaf, S. Djamel, O. Chouhal, H. Slimani, and R. Mahdaoui, "Robust control strategy for an electric water pump powered by the photovoltaic panel," in *2024 3rd International Conference on Advanced Electrical Engineering (ICAEE)*, IEEE, Nov. 2024, pp. 1–6. doi: 10.1109/ICAEE61760.2024.10783300.
[20] B. Yassine, Z. Fatiha, and L. Chrifi-alaoui, "Robust speed sensorless indirect field-oriented control of induction motor drive using LQR controller," *International Journal of Sciences and Techniques of Automatic Control & Computer Engineering*, vol. 9, no. 1, pp. 2013–2019, 2015.
[21] Y. Beddiaf, F. Zidani, L. Chrifi-Alaoui, and S. Drid, "Modified speed sensorless indirect field-oriented control of induction motor drive," *International Journal of Modelling, Identification and Control*, vol. 25, no. 4, pp. 273–286, 2016, doi: 10.1504/IJMIC.2016.076833.
[22] B. Yassine, Z. Fatiha, and L. Chrifi-Alaoui, "New MRAS approach for sensorless control of IM," in *2019 19th International Conference on Sciences and Techniques of Automatic Control and Computer Engineering (STA)*, IEEE, Mar. 2019, pp. 36–40. doi: 10.1109/STA.2019.8717287.
[23] C.-T. Chen, "A model-based direct adaptive PI controller for nonlinear process control," *Chemical Engineering Communications*, vol. 201, no. 9, pp. 1148–1172, Sep. 2014, doi: 10.1080/00986445.2013.803077.
[24] D. Rezzak, Y. Beddiaf, N. Boudjerda, M. C. Kihal, and M. Arbid, "Reset limited integral hysteresis sliding mode and hybrid MPPT/DC-bus controls with limits supervision in photovoltaic/valve-regulated lead-acid battery system," *Journal of Energy Storage*, vol. 112, p. 115507, Mar. 2025, doi: 10.1016/j.est.2025.115507.
[25] M. Gursoy, G. Zhuo, A. G. Lozowski, and X. Wang, "Photovoltaic energy conversion systems with sliding mode control," *Energies*, vol. 14, no. 19, p. 6071, Sep. 2021, doi: 10.3390/en14196071.
[26] R. F. Muktiadji *et al.*, "Control of boost converter using observer-based backstepping sliding mode control for DC microgrid," *Frontiers in Energy Research*, vol. 10, Mar. 2022, doi: 10.3389/fenrg.2022.828978.
[27] B. Torchani *et al.*, "Adaptive sliding mode control based on maximum power point tracking for boost converter of photovoltaic system under reference voltage optimizer," *Frontiers in Energy Research*, vol. 12, Oct. 2024, doi: 10.3389/fenrg.2024.1485470.
[28] R. Hamdi, Y. Beddiaf, and D. Sakri, "Design of an innovative vector control strategy for a photovoltaic-fed induction motor using a boost split-source inverter without MPPT," *International Journal of Advances in Signal and Image Sciences*, vol. 12, no. 2, pp. 1–21, May 2026, doi: 10.29284/s3058k14.

## BIOGRAPHIES OF AUTHORS



**Romaissa Hamdi** received the bachelor's degree in electrical engineering from Ababsa Abd Alhamid High School, Ain Beida, Algeria, in 2014. She received the master's degree in electrical engineering with specialization in electrical networks from Larbi Ben M'hidi University, Oum El Bouaghi, Algeria, in 2019. She is currently pursuing the Ph.D. degree in electrical control at Abbes Laghrour University, Khenchela, Algeria. Her research interests include electrical control, photovoltaic systems, fault diagnosis, and intelligent control. She can be contacted at email: hamdi.roumaissa@univ-khenchela.



**Yassine Beddiaf** received the bachelor's degree in electrical engineering in 1989, the M.Sc. degree in 1994, and the Ph.D. degree in electrical engineering in 2016 from the University of Batna, Algeria. He served as the Head of the Industrial Engineering Department at Abbès Laghrour University of Khenchela from 2012 to 2016 and has been a faculty member in the same department since 2014. Since 2021, he has held the rank of Associate Professor (Maître de Conférences Class A). His research interests include robust control of electrical systems, electric drives, renewable energy systems, artificial intelligence applications, and advanced control techniques. He can be contacted at email: beddiaf.yassine@univ-khenchela.dz.



**Djamel Sakri** is currently a faculty member with the Department of Electrical Engineering, Faculty of Science and Technology, Larbi Ben M'hidi University of Oum El Bouaghi, Algeria, and a researcher with the Laboratory of Electrical Engineering and Automatic (LGEA). His research interests include electrical machines, electric drives, sensorless control, predictive torque control, power electronics, and advanced control of induction motor systems. He has authored and co-authored several scientific publications in these research areas. He can be contacted at email: sk_djamel@yahoo.fr.



**Daoud Rezzak** received the Doctor of Engineering degree in electrical engineering. He is currently a researcher with the Department of Industrial Engineering, Faculty of Science and Technology, Abbès Laghrour University of Khenchela, Algeria. His research interests include power electronics, renewable energy systems, electrical power engineering, power converters, power system analysis, system modeling, and control of electrical energy systems. He can be contacted at email: rezzak.daoud@univ-khenchela.dz.



**Hassina Slimani** obtained the bachelor's degree in experimental sciences from Mohamed Seddik Ben Yahia High School, Skikda, Algeria, in 1995, and the State Engineer degree in electrotechnics, specializing in electrical control, from Badji Mokhtar University, Annaba, Algeria, in 2000. She is a researcher with the Laboratory of SATIT, Department of Electrical Engineering, Faculty of Science and Technology, Abbès Laghrour University of Khenchela, Algeria. Her research interests include electrical control, renewable energy systems, photovoltaic systems, fault diagnosis, and artificial intelligence applications in electrical engineering. She can be contacted at email: slimani.hassina@univ-khenchela.dz.